EUROPEAN ORGANIZATION FOR NUCLEAR RESEARCH

CERN–SPSC–2004–025
SPSC–M–723
21 September, 2004

C2GT: intercepting CERN neutrinos to Gran Sasso in the Gulf of Taranto to measure θ_{13}

A.E. Ball, A. Braem, L. Camilleri, A. Catinaccio, G. Chelkov, F. Dydak, A. Elagin, P. Frandsen, A. Grant, M. Gostkin, A. Guskov, C. Joram, Z. Krumshteyn, H. Postema, M. Price, T. Rovelli, D. Schinzel, J. Séguinot, G. Valenti, R. Voss, J. Wotschack, A. Zhemchugov

Abstract

Today's most challenging issue in accelerator-based neutrino physics is to measure the mixing angle θ_{13} which is known to be much smaller than the solar θ_{12} and the atmospheric θ_{23}. Yet establishing a finite value of θ_{13} is a prerequisite for observing CP violation in the neutrino mixing matrix. A deep-sea Cherenkov experiment with 1.5 Mt mass which utilizes the modified CNGS beam in off-axis geometry, is proposed in the Gulf of Taranto. The dominant beam component consists of monochromatic muon-neutrinos of 800 MeV energy. The favourable profile of the seabed allows for a moveable experiment at three different baselines around 1200 km. The experiment will observe the oscillatory pattern of muon-neutrinos with full amplitude, will measure θ_{23} and especially Δm^2_{23} with high precision, and will be sensitive to $\sin^2\theta_{13}$ as small as 0.0016 (90% CL; theoretical uncertainties excluded).

Memorandum submitted to the Villars 2004 meeting of the SPSC

Contact person: F. Dydak (*friedrich.dydak@cern.ch*)
http://home.cern.ch/dydak/C2GT_Villars_doc.pdf

Contents

1 Introduction, physics case

The oscillations of neutrinos and their non-zero mass may well be the first indication of physics beyond the standard model. The current explanation of the smallness of neutrino masses is the see-saw mechanism in which the small masses of the left-handed neutrinos that we observe are the counterpart of very heavy right-handed neutrinos. The study of the neutrino mass spectrum should therefore give us some insight into this domain of masses which are inaccessible to present-day accelerators. Furthermore, contrasting this mass spectrum to that of quarks should help us understand fermion masses in general. If CP violation is observed in the neutrino sector, it could lead to an explanation for the matter-antimatter asymmetry of the universe.

Limiting ourselves to three neutrinos, their oscillations can be described by the Maki, Nakagawa and Sakata (MNS) matrix. This is a 3 x 3 unitary matrix which can be described as a product of three independent rotations governed by three mixing angles $\theta_{12}, \theta_{23}, \theta_{13}$ which link the triplet of mass eigenstates (ν_1, ν_2, ν_3) to the triplet of flavour eigenstates $(\nu_e, \nu_\mu, \nu_\tau)$. The MNS matrix further permits a CP violation phase, δ (we ignore possible Majorana phases as they have no relevance for neutrino oscillations). In addition, for the modelling of neutrino oscillations, two independent squared-mass differences Δm^2_{12} and Δm^2_{23} need to be specified.

In a conventional parametrization [1], the MNS matrix U reads as follows:

$$U \equiv \begin{pmatrix} 1 & 0 & 0 \\ 0 & c_{23} & s_{23} \\ 0 & -s_{23} & c_{23} \end{pmatrix} \begin{pmatrix} c_{13} & 0 & s_{13}e^{i\delta} \\ 0 & 1 & 0 \\ -s_{13}e^{-i\delta} & 0 & c_{13} \end{pmatrix} \begin{pmatrix} c_{12} & s_{12} & 0 \\ -s_{12} & c_{12} & 0 \\ 0 & 0 & 1 \end{pmatrix}$$

with $s_{12} \equiv \sin\theta_{12}$, and similarly for the other sines and cosines.

The SuperKamiokande [2] data on atmospheric neutrinos are interpreted as oscillations of ν_μ into ν_τ. In a 3-flavour analysis [3], the 3σ range is $0.32 < \sin^2\theta_{23} < 0.70$ for $\sin^2\theta_{23}$, and $1.1 < \Delta m^2_{13} < 3.4 \times 10^{-3}$ eV^2 for Δm^2_{13} (since $|\Delta m^2_{12}| \ll |\Delta m^2_{23}|$, $\Delta m^2_{23} \cong \Delta m^2_{13}$).

The solar neutrino deficit is interpreted as an oscillation that depletes the original $\nu_{\rm e}$ signal in favour of ν_μ and ν_τ. The recent results of SNO [4] and KamLAND [5] have constrained the corresponding oscillation parameters to the hoped-for LMA solution (otherwise, CP violation in the neutrino sector would be out of reach). In a 3-flavour analysis [3], the 3σ range is $0.23 < \sin^2\theta_{12} < 0.39$ for $\sin^2\theta_{12}$, and $5.4 < \Delta m^2_{12} < 9.4 \times 10^{-5}$ eV^2 for Δm^2_{12}.

Only an upper limit is known for the angle θ_{13}. This has been set largely by the CHOOZ reactor experiment [6]. In a 3-flavour analysis [3], $\sin^2\theta_{13} < 0.05$, with a best fit around 0.01, well compatible with zero.

Thus, the atmospheric and solar neutrino results, when interpreted as neutrino oscillations, require non-zero neutrino masses.

The MINOS [7] experiment is expected to improve significantly the precision of Δm^2_{23} and θ_{23}. For example, Δm^2_{23} is expected to be measured at MINOS with an accuracy better than 10%. It is expected that MINOS will improve the CHOOZ limit on $\sin^2\theta_{13}$ by a factor of two only.

Today's major challenge is to determine the angle θ_{13}. If a finite value of the mixing angle θ_{13} is established, the next steps will be a measurement of the CP-violating phase δ and of the mass hierarchy. A Neutrino Factory appears to provide the right experimental conditions for these.

In the limit $|\Delta m^2_{12}| \ll |\Delta m^2_{23}|$, neutrino oscillation probabilities at planetary distances are well

described by only three parameters: θ_{23}, $\Delta m^2_{23} = \Delta m^2_{13}$, and θ_{13}. The leading terms are

$$\begin{aligned} P(\nu_{\rm e} \leftrightarrow \nu_\mu) &\cong \sin^2\theta_{23}\,\sin^2 2\theta_{13}\,\sin^2\left(\frac{1.27\Delta m^2_{23}\,L}{E_\nu}\right), \\ P(\nu_{\rm e} \leftrightarrow \nu_\tau) &\cong \cos^2\theta_{23}\,\sin^2 2\theta_{13}\,\sin^2\left(\frac{1.27\Delta m^2_{23}\,L}{E_\nu}\right), \\ P(\nu_\mu \leftrightarrow \nu_\tau) &\cong \cos^4\theta_{13}\,\sin^2 2\theta_{23}\,\sin^2\left(\frac{1.27\Delta m^2_{23}\,L}{E_\nu}\right), \end{aligned} \tag{1}$$

where the baseline L is measured in kilometres and the neutrino energy E_ν in GeV. For the energies and baselines considered in this paper, both the effects from the solar Δm^2_{12} and from matter effects in the Earth's crust can be neglected in good approximation.

With nearly 'bi-maximal' mixing seemingly favoured by Nature, with $\Delta m^2_{23} = 2.5 \times 10^{-3}$ eV^2 and with a small value of θ_{13}, Eqs. (1) reduce to

$$\begin{aligned} P(\nu_{\rm e} \leftrightarrow \nu_\mu) &\cong 2\sin^2\theta_{13}\,\sin^2\left(\frac{3.17\times10^{-3}\,L}{E_\nu}\right), \\ P(\nu_{\rm e} \leftrightarrow \nu_\tau) &\cong 2\sin^2\theta_{13}\,\sin^2\left(\frac{3.17\times10^{-3}\,L}{E_\nu}\right), \\ P(\nu_\mu \leftrightarrow \nu_\tau) &\cong \sin^2\left(\frac{3.17\times10^{-3}\,L}{E_\nu}\right). \end{aligned} \tag{2}$$

Among the transitions in Eqs. (2) the channels $\nu_{\rm e} \leftrightarrow \nu_\mu$ and $\nu_{\rm e} \leftrightarrow \nu_\tau$ are sensitive to θ_{13}. From the experimental point of view, the measurement of $\nu_{\rm e} \to \nu_\mu$ or – equivalently, when ignoring CP violation – $\nu_\mu \to \nu_{\rm e}$ oscillations is far superior to that of $\nu_{\rm e} \to \nu_\tau$ oscillations since the latter involves the detection of final-state taus. Before the advent of the $\nu_{\rm e}$ beam of a future Neutrino Factory, a possible experiment is to search for the sub-leading $\nu_\mu \to \nu_{\rm e}$ oscillation which could be present in addition to the leading $\nu_\mu \to \nu_\tau$ oscillation in a long-baseline experiment using a high-intensity ν_μ beam of conventional design.

The above is based on the assumption that the LSND claim [8] of a transition $\bar\nu_\mu \to \bar\nu_{\rm e}$ with $\Delta m^2 \sim 1$ eV^2 does not stand up to verification. If it does, a fourth neutrino is needed, which must be sterile since it is not seen in Z decay. Combined data analyses disfavour the notion of sterile neutrinos [3]. The MiniBooNE experiment will check the LSND claim. Throughout the following, the LSND result is ignored (admittedly a questionable attitude in the absence of a plausible alternative to LSND's interpretation of their result in terms of neutrino oscillations). The conservative point of view is taken that only the three known active neutrino flavours take part in neutrino oscillations.

As mentioned above, $\nu_\mu \to \nu_{\rm e}$ oscillations are sensitive to θ_{13}. However they are also, in the general case, sensitive to the mass hierarchy, the CP-violating phase δ, and the exact value of θ_{23}. Thus ambiguities introduced by these other effects must be taken into account when extracting a range of θ_{13} compatible with an experimental measurement of the probability of $\nu_\mu \to \nu_{\rm e}$ oscillations.

Before and in parallel to the project discussed in this paper, several other projects in Europe, the USA and Japan, have been proposed to address the measurement of θ_{13}, the mass hierarchy and CP violation. They will be discussed in Section 7.4.

2 Conceptual design

Measuring θ_{13} means measuring a small admixture of CC $\nu_{\rm e}$ events originating from the sub-leading $\nu_\mu \to \nu_{\rm e}$ transition. This is a long-baseline 'appearance' experiment. The uncertainties will be dominated by the statistics of the small number of signal events and by the intricacies of background events.

According to Eqs. (2), both $\nu_\mu \to \nu_\tau$ and $\nu_\mu \to \nu_{\rm e}$ oscillations have, for ν_μ with $E_\nu = 800$ MeV (this choice of energy will be motivated below) and for $\Delta m^2_{23} = 2.5 \times 10^{-3}$ eV^2, the first two maxima at $L \cong 400$ and 1200 km. At these baselines, the sensitivity to θ_{13} is maximal and the $\nu_\mu \to \nu_{\rm e}$ transition probability takes the simple form

$$P(\nu_\mu \to \nu_{\rm e}) \cong 2\sin^2\theta_{13}\ . \tag{3}$$

The precision of $\sin^2\theta_{13}$ is driven by the product of beam intensity and detector mass, on the condition that the background to the signal can be kept sufficiently small.

The neutrino energy of 800 MeV is well below the threshold of ~ 3.5 GeV for tau-production on nucleons, so there is no background from such events although nearly all ν_μ from pion decay have oscillated into ν_τ.

Background arises from flavour-blind NC events (which may serve a useful purpose for a cross-check of flux normalization, albeit limited by statistics). Another important background arises from genuine $\nu_{\rm e}$ from $\rm K_{e3}$ decays and from the decays of secondary muons in the decay tunnel of the neutrino beam.

The necessity of discriminating the small signal of CC $\nu_{\rm e}$ events from a potentially much larger background of NC events forbids a standard wide-band beam with its steeply falling energy spectrum. Instead, a narrow-band neutrino beam is needed, which permits such a discrimination by measuring the visible energy.

The off-axis geometry offers exactly this feature. The idea originated in 1993 at TRIUMF among a group of physicists, led by Helmer, who worked on what would evolve two years later into the E889 proposal to BNL. They discussed various options for creating a low-energy neutrino beam suitable to search for neutrino oscillations. They noticed that a detector located off-axis by a few degrees would intercept fairly monoenergetic neutrinos, in remarkable contrast to an on-axis location, without losing intensity at the preferred energy. The first published record is the write-up of a talk by Mann, who later became co-spokesman of the E889 proposal, together with Diwan and Helmer, given at the 1993 NESTOR Workshop [9]. A few months later, Helmer presented the idea at the 1994 Lake Louise Winter Institute [10]. The most detailed account is given in the 1995 E889 proposal [11] (which, however, was not finally approved).

A conventional neutrino beam originates primarily from the decay of charged pions which travel with the Lorentz parameters β, γ along the axis of the neutrino beam. The two-body decay into $\mu + \nu_\mu$ is isotropic in the pion rest frame. The longitudinal and transverse momenta of the ν_μ in the laboratory system are

$$\begin{aligned} p_{\rm L} &= \gamma(p^*\cos\Theta^* + \beta p^*) \\ p_{\rm T} &= p^*\sin\Theta^*\ , \end{aligned}$$

where $p^* = 0.03$ GeV/c is the neutrino momentum, and Θ^* is the polar angle of neutrino emission with respect to the pion direction of flight, all in the pion rest frame.

The polar angle Θ of neutrino emission in the laboratory frame is with $\beta \cong 1$

$$\Theta = \frac{R}{L} = \frac{1}{\gamma} \frac{\sin\Theta^*}{1 + \cos\Theta^*} ,$$

where R is the distance of the detector from the centre of the neutrino beam, and L the baseline.

It follows for perpendicular neutrino emission in the pion rest frame with respect to the pion direction of flight ($\Theta^* = 90°$) that

$$\Theta = \frac{1}{\gamma} .$$

The neutrino energy as a function of the detector's distance from the beam centre is

$$E_\nu(R) = \frac{2\gamma p^*}{1 + (\gamma \frac{R}{L})^2}$$

and has at the angle $\Theta = 1/\gamma$ half of the energy at the beam centre.

The neutrino flux per unit area and per pion decay is, as a function of the detector's distance from the beam centre,

$$\Phi_\nu(R) = \frac{\frac{\gamma^2}{\pi L^2}}{(1 + (\gamma \frac{R}{L})^2)^2} ,$$

and has at the angle $\Theta = 1/\gamma$ one quarter of the intensity at the beam centre.

The most important kinematic property of the neutrino beam is that at the angle $\Theta = 1/\gamma$ the neutrino energy is in first approximation independent of the energy of the parent pion:

$$\frac{\partial E_\nu}{\partial \gamma} = 0 .$$

This means that monoenergetic neutrinos are produced by a range of parent-pion momenta around the nominal momentum, thus opening the way to a monoenergetic neutrino beam with high intensity. For this reason, the corresponding $\gamma = 1/\Theta$ is referred to as 'magic'.

In contrast to ν_μ from pion decay, background neutrinos e.g. from Kaon decay do not obey the same kinematics and exhibit at the angle $\theta = 1/\gamma_\pi$ a broad energy spectrum.

The cross-section of 800 MeV neutrinos on nucleons is only known to within some 20%. More than 50% of the interactions are quasi-elastic, i.e. the final-state electron carries nearly the full initial neutrino energy. Therefore, the signal are forward-going 800 MeV electrons, which lend themselves – especially when combined with the requirement of a very large target mass – to detection in a water Cherenkov detector.

Nature has kindly provided a nearly 600 km long underwater trench of minimal depth 1000 m, starting in the Gulf of Taranto in the south of Italy and extending through the Ionian Sea to the Greek coast. Moreover, the trench is aligned with the CNGS beam axis. Figure 1 shows the map of the Gulf of Taranto including the profile of the sea bed and the vertical projection of the CNGS beam axis. Only some 10 – 20 km west of the projected CNGS beam axis the trench reaches its maximum depth. There, an underwater detector could be moved at a depth of 1000 m without obstruction close to the projected CNGS beam axis, over hundreds of kilometres. For illustration, points A, B, and C in Fig. 1 denote locations vertically below the CNGS beam axis at a distance from CERN of 1150, 1200, and 1250 km, respectively. However, any distance from CERN between 1100 and 1700 km is possible with a minimal depth of 1000 m.

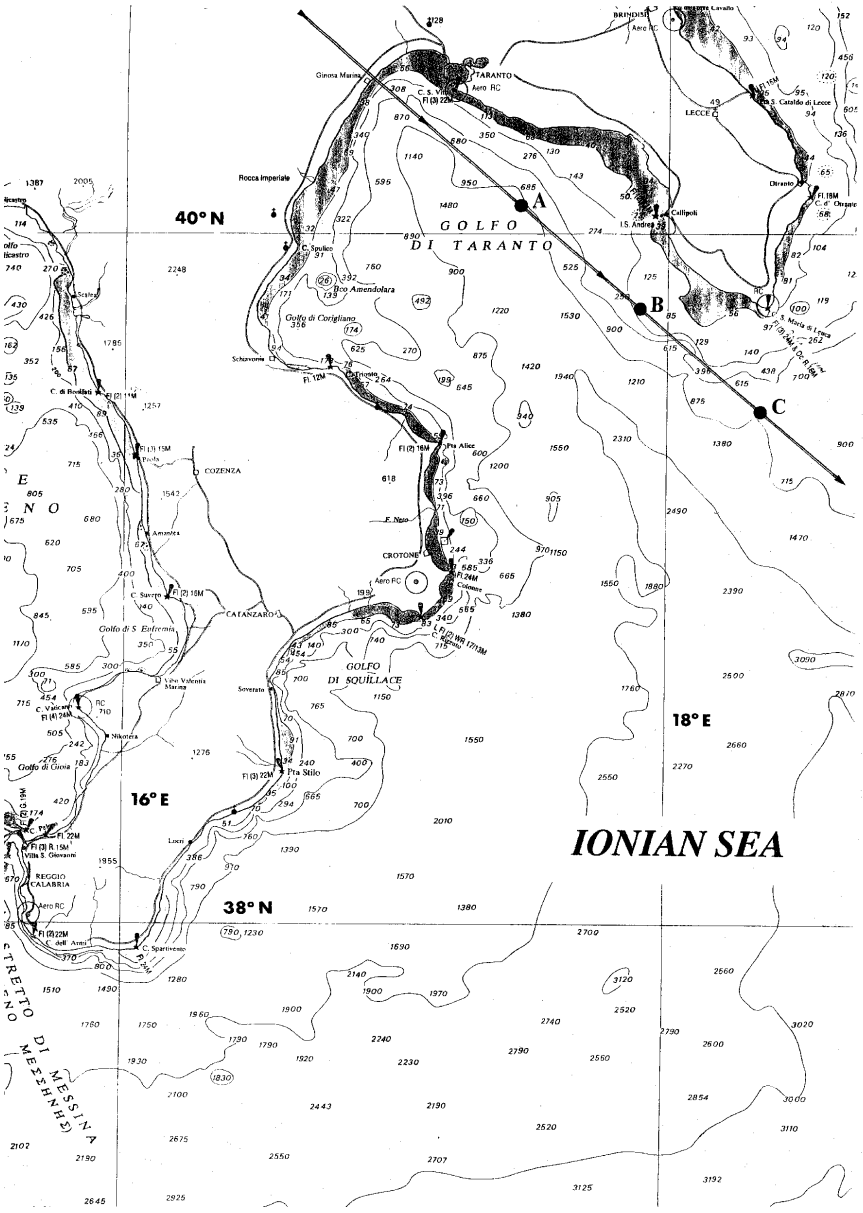

Figure 1: Map of the Gulf of Taranto; for illustration, the points A, B, and C below the CNGS beam axis denote locations spaced by 50 km, with B at a distance of 1200 km from CERN.

Incidentally, a depth of 1000 m is needed to shield PMs against daylight [12].

Since the incoming neutrinos have a well-defined direction, an underwater vertical 'disc' perpendicular to the beam direction is the most suitable detector geometry. The useful depth along the beam is limited by the light attenuation length. Taking into account the Cherenkov angle in water of $\sim 42°$, the fiducial volume has the shape of a truncated cone. The disc is constructed as a grid of regularly spaced photosensors which record the Cherenkov light of forward-going 800 MeV electrons from CC quasielastic $\nu_e$events.

At a distance of 1200 km, considered as reference baseline in this paper, the centre of the CNGS

beam is already 44 km above the detector. This defines the 'magic' angle $1/\gamma_\pi$, which in turn fixes the monochromatic neutrino energy from pion decay at this location to be 800 MeV – incidentally the energy required for the second oscillation maximum for $\Delta m^2_{23} = 2.5 \times 10^{-3}$ eV^2. For illustration, the resulting oscillatory amplitude for off-axis neutrinos is given in Fig. 2 as a function of the baseline, for $\Delta m^2_{23} = 2.5 \times 10^{-3}$ eV^2 and for $\Delta m^2_{23} = 1.0 \times 10^{-3}$ eV^2. For baselines smaller than 1200 km, the neutrino energy is considered constant since a potential detector would be located on the line where the cone with opening angle $1/\gamma_\pi$ intersects with the surface of Italian soil; the neutrino energy equals the one at 1200 km. Beyond 1200 km, the oscillation is faster because of the combined effect of increasing the baseline and reducing the neutrino energy when moving downstream and thus increasing the off-axis angle because of Earth's curvature. Independently of Nature's precise choice of Δm^2_{23}, the detector locations sample well the oscillatory pattern and thus offer maximum sensitivity to the oscillation parameters.

For $\Delta m^2_{23} = 2.5 \times 10^{-3}$ eV^2, the next oscillation minimum occurs already at a baseline of $\sim$ 1300 km. Moving the detector downstream by some 100 km, both the leading and subleading oscillations are switched off: all $\nu_\mu \to \nu_\mathrm{e}$ and $\nu_\mu \to \nu_\tau$ transitions have disappeared, the full flux of ν_μ is restored. The CC ν_μ events can be recorded through the quasi-elastic channel in the water Cherenkov detector nearly as easily as the CC quasielastic ν_e events.

Therefore, the experiment will unambiguously demonstrate the oscillatory pattern and the transition of one neutrino flavour to another, just by moving the detector from one location to another which is some 100 km downstream.

The position halfway in between, at some 1250 km, has maximum sensitivity to Δm^2_{23} and lends itself to its precise measurement.

The expected physics result is a high-precision measurement of θ_{23} and especially Δm^2_{23}, and a high-sensitivity search for a non-zero θ_{13}.

The data taking campaign will last about eight years.

Today, Δm^2_{23} is only known to $\sim 50\%$ and therefore the precise location of the oscillation maximum is not known. However, this does not invalidate the argument that a detector movement of order 100 km will explore the oscillatory pattern with high sensitivity.

3 The CNGS beam in off-axis geometry

Table 1 summarizes beam and detector parameters 1000 m below sea level, for a detector location in the Gulf of Taranto 1200 km from CERN.

Figure 3 shows the dependence of the neutrino energy E_ν on γ_π at a distance of 1200 km from CERN and a distance of 44 km from the CNGS beam axis, i.e. at an off-axis angle $\theta = 1/27.1$ rad. The important feature of the spectrum is its broad maximum at $E_\nu \sim 800$ MeV, which leads to a nearly monochromatic neutrino beam, essential for the goal of the experiment.

The CNGS beam [13] will be employed, with unchanged geometrical layout and with unchanged incident proton momentum of 400 GeV/c. However, target, horn and reflector need to be redesigned with a view to optimizing the flux of 3.8 GeV pions parallel to the axis of the decay tunnel.

The attractive feature of the off-axis geometry is that a broad band of pion momenta around 3.8 GeV/c, between 2 and 8 GeV/c about, is useful and yet leads to a nearly monoenergetic

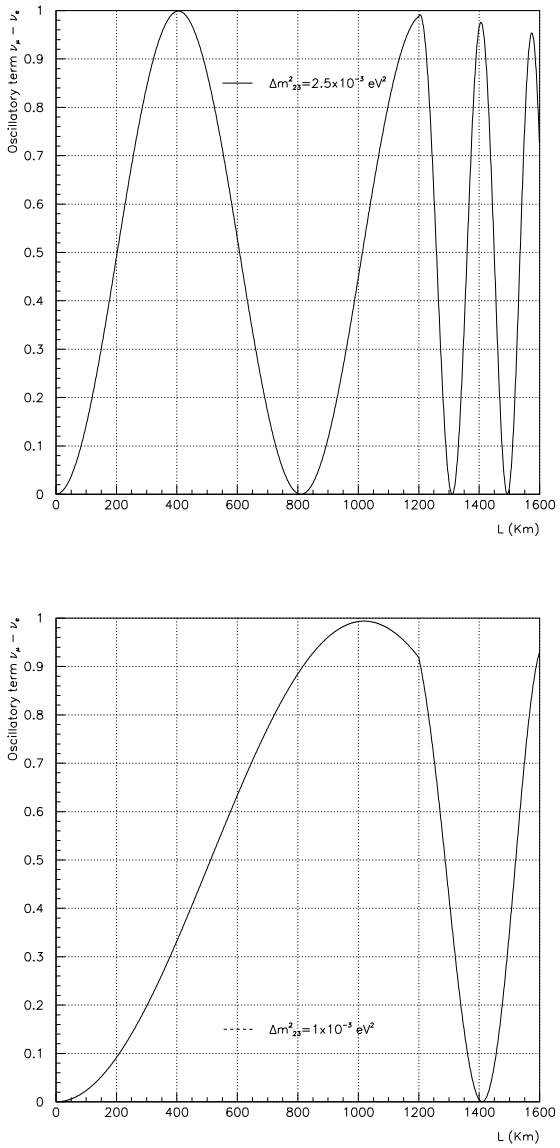

Figure 2: Oscillatory amplitude for off-axis neutrinos as function of the baseline, for $\Delta m^2_{23} = 2.5 \times 10^{-3}$ eV^2 (top), and for $\Delta m^2_{23} = 1.0 \times 10^{-3}$ eV^2 (bottom). For baselines smaller than 1200 km, the neutrino energy is constant and equals the one at 1200 km.

neutrino beam.

Needless to say the highest possible intensity of the neutrino beam is required. Maximizing the number of pions requires a careful optimization of the target length (for efficient transfer of the energy of the incoming proton to low-momentum pions) and of the target thickness (to help the escape of useful pions from the target).

Figure 4 shows the results of a FLUKA study of the yield of π^+ and π^- from rotationally symmetric graphite targets with different absorption lengths and radii. It appears that a target

Table 1: Parameters of neutrino beam and detector for a distance of 1200 km from CERN.

Distance L from CERN [km]	1200
Geodesic longitude	017° 54' E
Geodesic latitude	39° 47' N
Radial distance R from CNGS beam axis [km]	44
γ of parent pion	27.1
Parent-pion momentum [GeV/c]	3.8
Neutrino flux per decaying pion [cm^{-2}]	4.1×10^{-15}
Neutrino energy from pion decay [GeV]	0.81
Neutrino energy from Kaon decay [GeV]	3.4

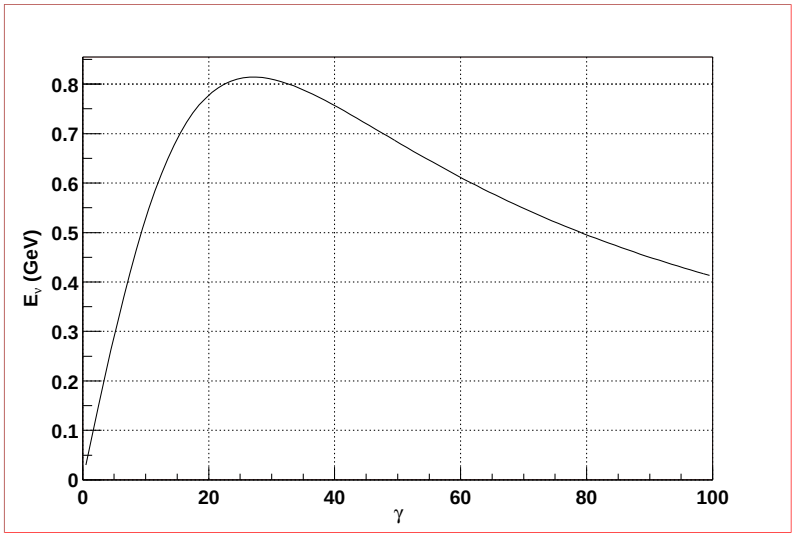

Figure 3: Neutrino energy from pion decay as a function of γ_π at an off-axis angle $\theta = 1/27.1$.

of four absorption lengths (152 cm) and a radius of 2.5 mm is well suited. The yield of ~ 3.3 π^+ per proton with momenta between 2 and 8 GeV/c and polar angle ≤ 200 mrad is used to estimate the neutrino flux.

The main device for focussing the pions to an angle of less than a few mrad with respect to the beam axis is a magnetic horn. Its design must respect practical constraints: outer radius not exceeding 0.75 m, length not exceeding 10 m, and current not exceeding 250 kA. With 'ideal' horn focussing, out of the initial 3.3 π^+ per proton, 1.5 can be bent parallel to the horn axis.

Additional help toward maximizing the number of useful π^+ is provided by a reflector with a horn-like shape, but at greater distance from the target.

The flux delivered by a combined optimization of target, horn and reflector, yet in a technically realistic configuration, is expected to yield 0.5 useful pion decays per 400 GeV/c proton incident on the target.

Figure 5 shows a simulation [14] of the ν_μ flux from the decay of pions and Kaons from 400 GeV

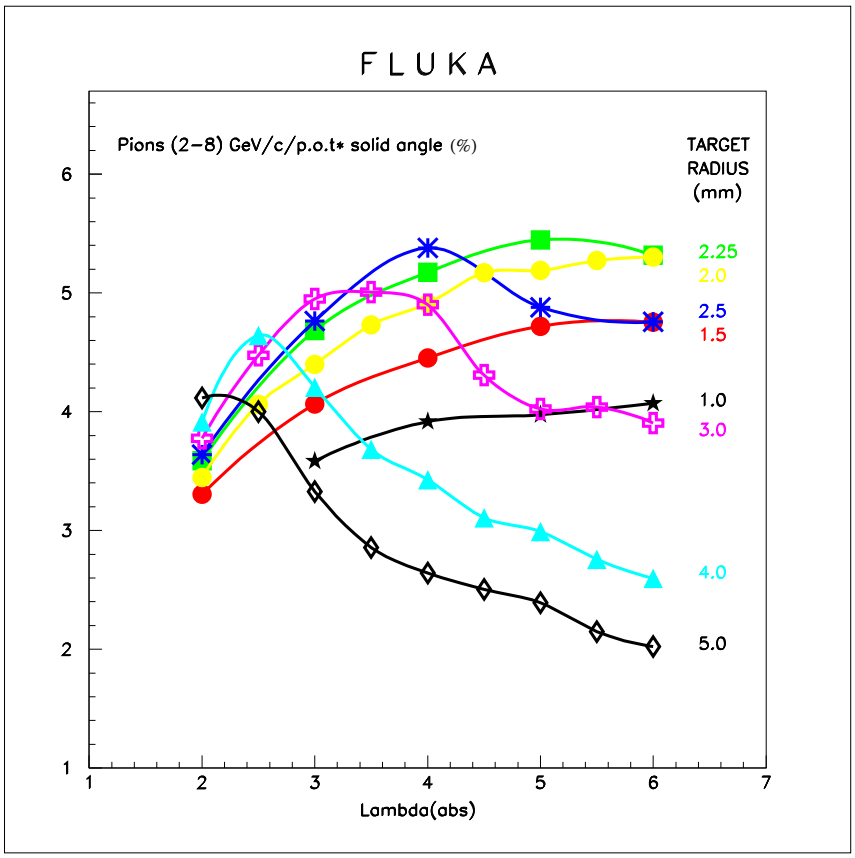

Figure 4: Yield of $\pi^{\pm}$ from rotationally symmetric graphite targets with different absorption lengths and radii.

proton interactions, with full longitudinal momentum variation yet with the transverse momentum set artificially to zero. Neutrino oscillations are assumed to be absent. The monochromatic line of 0.8 GeV ν_μ from pion decay, due to the off-axis geometry is apparent.

The decay tunnel of the CNGS beam is 1 km long. This length gives also rise to background from decays of secondary muons. The ν_e contamination shown in Figure 5 includes this source of genuine ν_e.

Figure 6 show the cross-sections of various processes as generated by the program NEUGEN [15].

4 Detector design: mechanical structure

The detector consists of a grid of Optical Modules (see Section 5) mounted on a large square structure. The structure is located at a depth of 1000 m perpendicular to the neutrino beam. Apart from shielding the daylight, this depth of is beneficial for obtaining good water transparency. The structure is anchored to the sea bed during data taking. All data acquisition is local and centred in a counting house on a service vessel. The structure is designed so that it

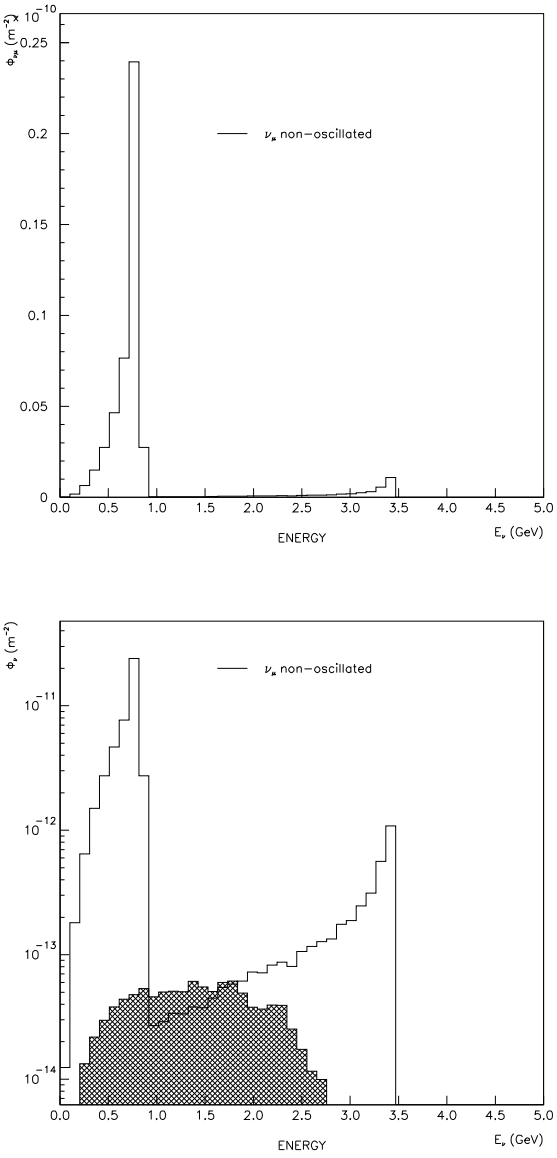

Figure 5: Energy spectrum of the flux of ν_μ from the decay of pions, charged and neutral Kaons, and secondary muons, with full longitudinal momentum variation but with zero transverse momentum; the hatched area shows the $\nu_{\rm e}$ contamination; neutrino oscillations are assumed absent; linear scale (top) and logarithmic scale (bottom).

can be moved to different positions in the Gulf of Taranto.

The detector technology is inspired by SuperKamiokande and by the pioneering R&D work done by the DUMAND, LAKE BAIKAL, ANTARES, NEMO and NESTOR Collaborations.

In this Section we indicate how the mechanical support structure of the detector disc might be constructed and discuss how such a structure can be deployed, and maintained, at the experimental site. For this study, a square plane of dimension 300 m $\times$ 300 m has been considered

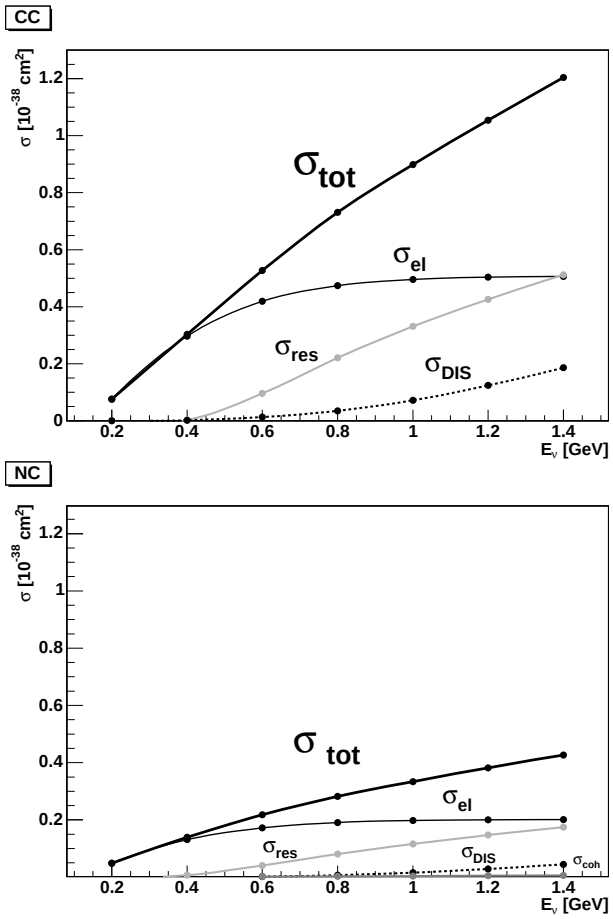

Figure 6: CC (top) and NC (bottom) cross-sections per nucleon, as a function of the neutrino energy, as generated by the program NEUGEN.

of which the area with radius less than 150 m is instrumented with Optical Modules.

We have had neither the time nor the expert manpower to explore technical details, or do any optimization. However, we believe that we have a feasible solution at hand.

Sea water is notorious for being very corrosive. The designers of ANTARES and NESTOR have chosen to use Titanium (Ti) as the main metal in contact with seawater. Hence all our calculations are based on the use of this material, however, if sufficiently good surface protection can be found, the use of more traditional materials like steel and aluminum, or of special aluminum alloys (generally in the 5000 series) should also be investigated.

4.1 Conceptual considerations

It is proposed to construct the detector plane from a number of Mechanical Modules. They are bolted rigidly together and designed so that their composite structure has sufficient rigidity against water currents and individual Mechanical Modules can be safely handled. Rows of Mechanical Modules are attached together by divers just below the surface of the sea. After the first row of modules is complete the mooring system is installed, the first row is lowered to

greater water depth and the next row is attached. This process is continued until the full 300 m $\times$ 300 m square plane is constructed.

The detector is equipped with a 'robot' to extract, and bring to the surface a Mechanical Module in order to repair or replace its components.

4.1.1 Estimation of structure dimensions

Firstly, we estimate the force acting on the whole 300 m $\times$ 300 m structure. The ANTARES Collaboration uses a maximum water velocity of 10 cm/s in their designs which is considered conservative. From the point of view of water resistance our structure can be imagined as constructed from a series of tubes of the order of 10 cm diameter and from spheres of several hundred millimetres diameter. With water velocity of 10 cm/s these dimensions correspond to Reynolds numbers of between 6000 and 30000. In this regime of Reynolds number it is legitimate to use the formula

$$F_{\mathrm{D}} = \frac{1}{2} C_{\mathrm{D}} \rho u^2 A$$

for the force [16], where ρ is the water density, u the water velocity, A is the area presented normal to the water flow direction and C_{D} the drag coefficient. For the tube and sphere diameters under consideration a value of $C_{\mathrm{D}} = 1$ is somewhat conservative. Assuming that the effective area is 30% of the full 300 m $\times$ 300 m, we arrive at a total estimated force of 135 kN.

The plane will deform under such a pressure. In order to estimate the quantity of material needed we must define how much deformation is tolerable. We consider the simple 2-dimensional problem of a strip of Ti material, 300 m long and one metre wide. We subject this to a pressure of 135 kN/(300 m $\times$ 300 m) and assume that the beam is only supported at each end. The bending at the ends is given by

$$\theta_{\max} = \frac{w_{\mathrm{a}} L^3}{24 E I} \, ,$$

where w_{a} is the load per unit length, L is the beam length (300 m), E is the Young's modulus of the material (116 GPa for Ti) and I is the moment of inertia of the cross-sectional area. Taking a maximum permissible angular deflection of 0.05 rad we can calculate the necessary moment of inertia. We can translate this moment of inertia from a 1 m strip of material into some sort of tubular structure. As our baseline we shall consider that each rectangular Mechanical Module is bounded on each side by a tubular truss structure consisting of three longitudinal Ti tubes arranged on an equilateral triangle and cross-braced for rigidity. The connections between adjacent Mechanical Modules need to be designed so as to ensure that the 300 m long beam has continuous properties. For the triangular structure proposed the moment of inertia can be approximated by

$$I = 2A \left(\frac{L}{2} \right)^2 \, ,$$

where A is the cross-sectional area of one of the tubes and L is the side of the equilateral triangle. Although the bending moments in the 300 m $\times$ 300 m structure do not vary greatly over the whole plane, the shearing forces are a maximum at the four corners where the structure is attached to the mooring ropes. We have calculated that the forces (particularly the buckling forces) can be withstood using a truss structure made from tubes of diameter approximately 10 cm and with a distance between the longitudinal tubes of the triangular structure of the order of a couple of metres.

Altogether, we consider that the detector, taken as a continuous structure, is subject to relatively gentle forces and can be made with a reasonable amount of material. However, we also have to

demonstrate that the sub-components from which this structure is composed, the Mechanical Modules in particular, can be made sufficiently rigid to be handled (e.g. transport from the point of insertion of the optical elements to the detector deployment site, lowering into the sea at the deployment site, attachment of the Mechanical Module to its neighbours etc.). Such considerations limit the Mechanical Module size to approximately 10 m × 10 m which we adopted as our baseline.

We have performed both analytic and finite element calculations and find that the total weight of the structure would be of the order 500 t; this includes the structural material itself and the addition material for the cross-bracing.

4.1.2 Mechanical Module construction

The Mechanical Module is surrounded by a structural frame with triangular cross-section. Figure 7 shows the example of a 10 m × 10 m Mechanical Module together with its Optical Modules.

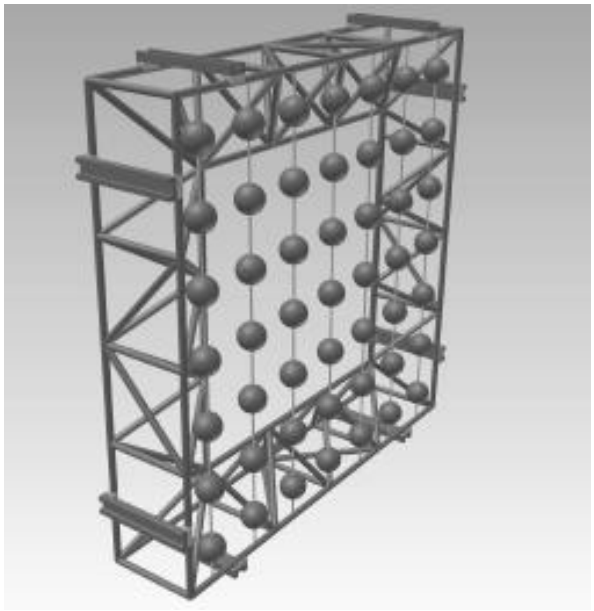

Figure 7: A 10 m × 10 m Mechanical Module with Optical Modules arranged in vertical strings; each side has two guides that locate the Mechanical Module with respect to the framework located between Mechanical Modules.

For each Mechanical Module all its service cables can be directed to the surface. If, for example, the Mechanical Module is 10 m × 10 m, there would be 30 service cables exiting at the top of a column of Mechanical Modules. One of the vertical sides of each Mechanical Module would be equipped with 30 cable channels. When all the Mechanical Modules are assembled together the cables channels form 30 continuous vertical channels per column of Mechanical Modules. Each Mechanical Module has thus an individual channel in which its service cable runs. In addition, there is a rail on which the service robot will run.

The equipped Mechanical Module should be nearly neutrally buoyant. With our present con-

struction, the upthrust provided by the spheres containing the photo-detectors will exceed the weight of the tubing and hence some extra ballast will have to be provided to make it sit upright in the water.

4.2 Deployment

The first equipped Mechanical Module is lowered vertically from the service vessel into the sea until its upper part is located a few metres below the surface of the sea. At this early stage of detector assembly, the mooring devices have not yet been installed. In the event of heavy weather, and until the final mooring system is installed, provision has to be made for lowering the partially assembly detector to a safe depth – i.e. with the upper part of the partially assembled device not less than 50 m below the surface.

The second Mechanical Module is then lowered into the water and positioned near the first. The two Mechanical Modules are separated by a vertical column that incorporates the cable channel. Similar devices on the top side (but without the cable channel) make up a rigid frame around the Mechanical Modules. Divers assemble the two Mechanical Modules and their associated intermediate frame elements.

The fastening procedure is repeated until a full row of 30 Mechanical Modules is floating below the surface of the sea.

Figure 8: Mooring system (not to scale, simplified); note the bifilar suspension; the upper mooring system which completes the stabilization of the structure, is not illustrated.

At this stage the first part of the mooring system is deployed. At a distance of about 200 m from one end of the partially assembled detector and at an equivalent distance from the surface of the plane of Mechanical Modules, a ship lowers a heavy (100 t) block down to the seabed by means of a cable. Once this block is positioned on the seabed the end of the cable is passed

through a pulley situated at the end of the lower side of the row of Mechanical Modules. From here the cable passes through a similar pulley on a second heavy block. This, in turn, is lowered to the sea bed, again some 200 m from the end of the row of Mechanical Modules, but on the opposite side of it (see Fig. 8). The free end of the cable is attached to a winch in a buoy that floats vertically above the second mooring block. Thus, when the operation is finished the cable, which is initially fixed to the first block, goes up to pass through the pulley on the end of the detector, descends again to pass through the pulley on the second block and finally goes up and is attached to a winch in the buoy. The operation is then repeated at the other side of the partially assembled detector. The detector is now attached to a bifilar system that gives it positional stability. The device can now be positioned at any depth by activating the winches in the buoys. In order for this operation to be effective, each Mechanical Module has to have slight buoyancy.

At this point the single row of Mechanical Modules is lowered (using the winches) until the tops of the Mechanical Modules are some 20 metres below the surface of the sea. Mechanical Modules for the second row are then lowered one by one into the sea. Divers secure each Mechanical Module to the neighbours beneath and to the side of it. At this time the cable from the lower neighbour is run up the channel described above (in fact, as successive layers are installed there will be more and more cables to fit in the channels). After the second layer is installed, the operation is repeated for successive layers.

4.3 Maintenance

From time to time elements of the detector will have to be repaired or maintained. Servicing of the electronic components and replacement of optical modules can realistically only be done on the surface. We have adopted the policy that the smallest serviceable unit is the Mechanical Module.

Using the mooring system the detector is raised from its working depth of 1000 m up to the servicing position in which the tops of the uppermost Mechanical Modules are a few metres below the surface of the sea. The service robot is then lowered into the sea and is fixed, by divers, to the rails attached to the uppermost Mechanical Module in the column containing the Mechanical Module to service. The service robot moves down the rail and stops when it is opposite the Mechanical Module that needs to be serviced. Once in position the service robot is located with positioning pins and clamped in place.

Using remote handling equipment the fasteners attaching the Mechanical Module to its neighbours are released and the Mechanical Module is pulled out of the plane of the detector and into the service robot. To carry out this operation the Mechanical Module and the service robot are fitted with locating rails.

With the Mechanical Module securely in place preparation for the ascent of the service robot to the surface begins. The positioning pins and clamps are released and the robot starts to move. As it goes up a "finger" releases the Mechanical Module's cable from its channel. The cable is pulled into the Mechanical Module and stored (provision has to be made for storing up to 300 m of cable in the Mechanical Module). When the robot and its contents reach the top of the detector (i.e. opposite the top Mechanical Module) divers release the service robot from the rails. It can now be raised to the service vessel. Since the cable is attached to the top of the detector, it should be noted that during this final ascent from the top of the detector to the service vessel, cable would be paid out from the service robot.

5 Detector design: the Optical Module

5.1 Conceptual considerations

Although a large number of Cherenkov photons is generated, there is a rapid fall-off of the number of photons with distance such that at distances beyond 50 m from the detector plane, only a few photo-electrons would be produced in a photo-detector that had an, as yet unachievable, area of 1 m^2. For this reason, in the first descriptions of the detector, the light collecting efficiency was augmented by the use of rotationally symmetric parabolic mirrors, optimized for the collection of light under the Cherenkov angle of incidence (42°). It was realised, however, that the angular response function of such mirrors was too strong a function of the angle of

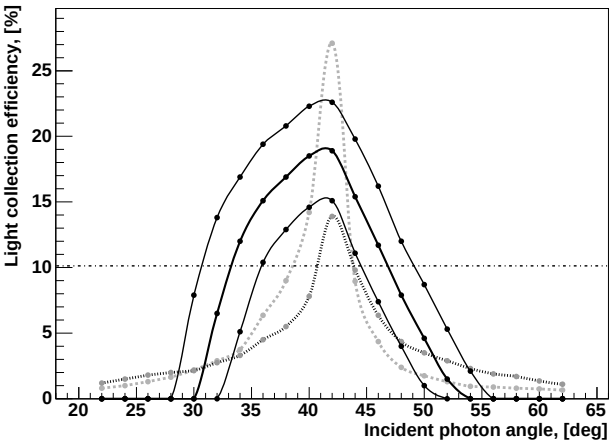

Figure 9: Angular response functions: the three continuous lines show the light collection efficiency of a parabolic mirror system with photodetectors with diameter 40, 50 and 60 cm, respectively; in our simulations, a flat light collection efficiency of $\sim 8\%$ was used; for comparison, also the angular incidences of photons from 800 MeV electrons (dotted, dark) and muons (dotted, light) are shown.

incidence of the Cherenkov light with respect to the mirror axis (see Fig. 9). As a consequence of this, certain signatures of the events, such as the 'fuzziness' of rings produced by electrons, would suffer. More seriously, in the case of a $\pi^0 \to 2\gamma$ decay there is a chance of missing one of the rings completely. Hence the mirror concept was abandoned in favour of Optical Modules with a flatter angular response function.

We note in passing that we also considered a different detector type based on photon conversion in wavelength-shifting fibres. That was motivated by the abundance of UV photons in Cherenkov radiation. However, that concept proved inefficient since the salt in sea water makes it opaque for UV photons (see Section 6).

Our simulations use the measured light transmission in the Mediterranean Sea and the quantum efficiency of bi-alkali photo-cathodes (both as a function of wavelength). These simulations indicate that, if the size and distribution of the photo- detectors is such as to cover $\sim 8\%$ of the surface area of the detector plane (the lower limit seems to be $\sim 4\%$), the experiment is feasible.

The Optical Modules can be realized with 20" photomultipliers (with an approximately flat

photocathode) on a square grid with a side of ~ 1.6 m.

The design of the Optical Module is driven by the scientific requirements and the special environmental conditions:

- efficient light detection in the wavelength range 300 – 550 nm;
- maximal surface and angular acceptance;
- sensitivity to a single photoelectron;
- timing resolution ≤ 2 ns;
- dark count probability ≤ 0.1 photoelectron within a time window of 100 ns;
- operation in sea water at a depth of ~ 1000 m.

Driven by these specifications, but also by considerations of cost, we embarked on our own concept of an Optical Module. It consists of a large, almost spherical, Hybrid Photon Detector (HPD), inserted in a spherical glass container which withstands high pressure.

We have chosen the HPD technology [17] rather than a conventional photomultiplier tube because it provides very clean signal characteristics and uniform collection efficiency for even large angles of photon incidence.

5.2 The Hybrid Photon Detector

5.2.1 Design

Our HPD design is schematically shown in the upper part of Fig. 10. It is based on a spherical envelope of borosilicate glass of 380 mm outer diameter (wall thickness about 5 mm).

The bottom part of the glass envelope is sealed by a metallic baseplate, which supports the silicon sensor (see below) and is equipped with electrical feedthroughs. A semi-transparent bialkali photocathode (quantum efficiency $\approx$25% at 400 nm) is best suited for the near-UV and visible wavelength range. It covers the inner glass surface down to the shaper electrode.

The photoelectrons are accelerated in the radial electric field between the cathode and the silicon anode. Electrostatic simulations predict a uniform angular acceptance of about $\pm 110^\circ$ with a transit time spread below 1 ns. The photocathode is maintained at negative high voltage ($U_\mathrm{C} = -20$ kV), while the Si sensor is grounded. The charge gain of the detector is given by the number of electron-hole pairs, which are produced when a photoelectron is stopped in the Si sensor: $G = e \cdot U_\mathrm{C}/3.6\ \mathrm{eV} \approx 5000$. The dissipative nature of this gain mechanism leads to a well defined signal with fluctuations generally below the pedestal noise of the readout electronics (see below) and allows for photoelectron counting up to at least five photoelectrons. The large angular coverage is achieved by arranging the anode as five individual silicon sensors of 15 mm $\times$ 15 mm size, mounted edge-to-edge on a ceramic support cube. The bottom face of the cube sits on an insulated cylinder which is mounted on the baseplate. The cube is surrounded by a round field cage of about 30 mm diameter, which is largely transparent to the photoelectrons. Its rôle is to reduce the electric field gradient in the vicinity of the silicon sensor to values which exclude electric discharges from the silicon surfaces.

The HPD is insensitive to the Earth's magnetic field.

Since the HPD's sensitivity does not change with the angle of photon incidence, the angular response (see Fig. 9) is not flat but increases with angle of incidence. Hence, taking into account the increase at the Cherenkov angle, we need one Optical Module per 1.5 m distance or 2.25 m^2 area to achieve a light collection efficiency of $\sim 8\%$.

This granularity leads to a total of 32000 Optical Modules.

5.2.2 The high-pressure container

The HPD is housed in a standardized high-pressure glass container as used by the fishing industry. The 380 mm HPD fits in a 17-inch container with a gap of 1 cm. The lower part of the container provides sufficient space for a compact HV supply, readout and calibration electronics. Industrial pressure and sea-water proof feedthroughs permit electrical supply, control and readout of the Optical Module.

The optical and mechanical contact between the HPD and the container is ensured by an optical gel with matched refractive index (the gel also diminishes the vacuum volume, thus reducing the shock wave in water generated by an imploding Optical Module).

A 3D schematic of the Optical Module is shown in the lower part of Fig. 10.

5.2.3 The readout electronics

The relatively small signal amplitude (1 fC) and the required timing precision ($\leq$ 2 ns) call for a low noise front-end followed by a pulse shape digitization unit. We aim for a signal-to-noise ratio of about 10 for single photoelectrons, i.e. the pedestal noise must not exceed 500 e^- (RMS). A front-end with 100 ns shaping time is able to achieve noise levels of the order 25 – 30 e^-/pF. The above-mentioned silicon sensors are therefore segmented in 4 or 9 cells such that the capacity per cell drops well below 20 pF each. All cells are read out by a single chip. Waveform digitization is performed at a rate of about 300 MHz.

An alternative approach is to equip the HPD with an avalanche silicon diode, commonly used as avalanche photodiode (APD). This leads to a conveniently large signal amplitude ($\approx 10^5$ e^-), as the HPD 'bombardment' gain is augmented by the avalanche gain. However, the specific detector capacitance of avalanche diodes (300 – 1500 pF/cm^2) and the non-availability of large diodes ($> 5 \times 5$ mm^2) pose stringent limitations believed to be incompatible with a large-size HPD.

5.2.4 A reduced-scale prototype

Considerable experience exists at CERN in the design and construction of high-performance HPD's. The existing CERN facilities [18] allow to build a prototype HPD of the above type with an outer diameter of about 210 mm. A large part of the equipment is available from previous developments. The reduced-scale prototype allows to verify most of the HPD's characteristics, including sensitivity, electrostatics and signal characteristics.

Although the HPD seems a very attractive device, we will continue to study possible alternatives.

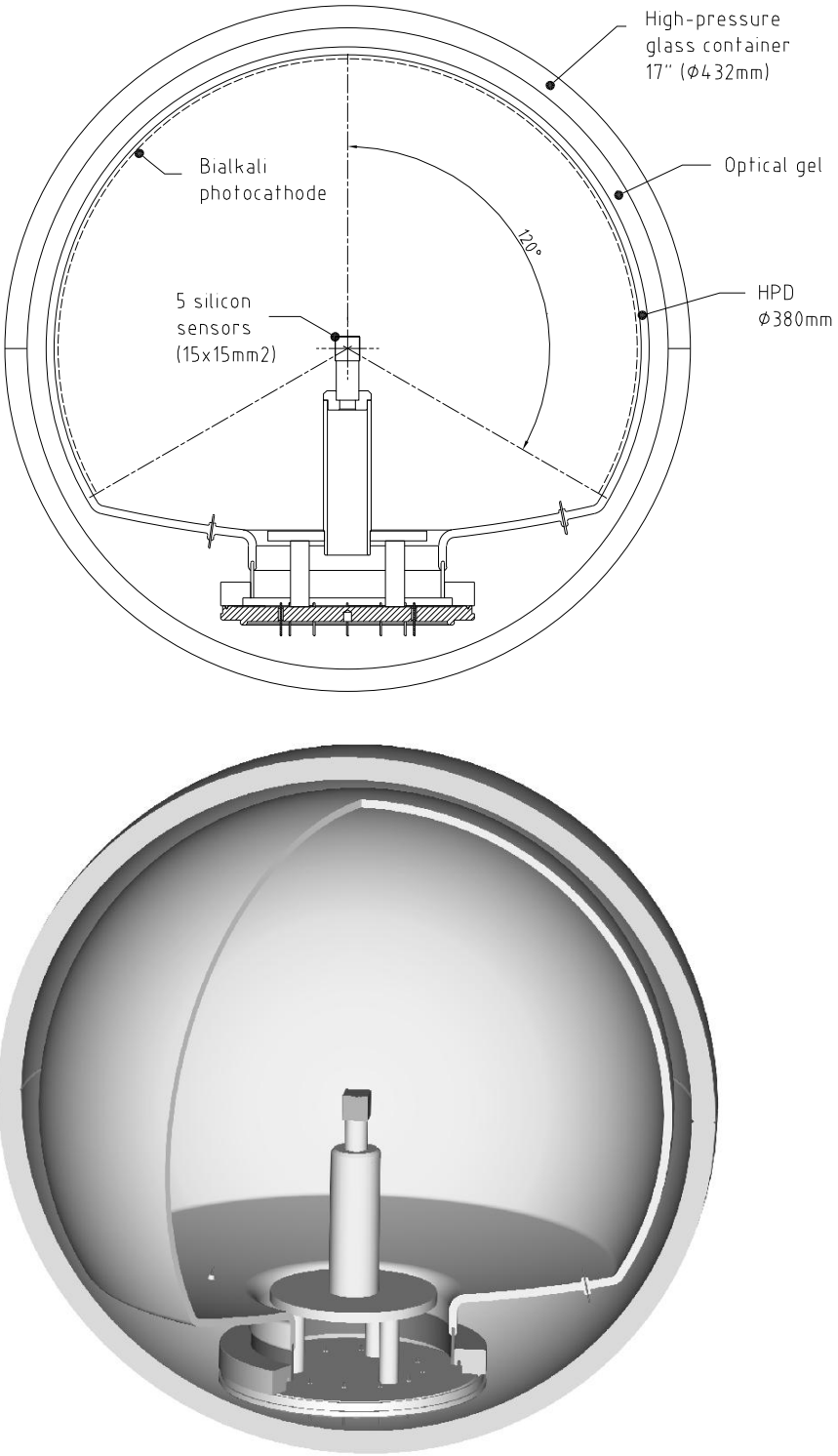

Figure 10: Schematic view of the Optical Module (top), 3D schematic of the Optical Module (bottom).

6 Simulation results

We have set up a simulation of the experiment based on GEANT4, with a view to simulating the detector response to various types of events, to evaluate detector properties like resolution of measured physical quantities, signal efficiency and backgrounds. Another goal was to understand important design parameters like granularity and sensitivity to Cherenkov photons.

Since the central aim of the experiment is to measure quasielastic events from the interactions of ~ 800 MeV ν_e and ν_μ, many simulation results will refer to electrons and muons with average total energy 800 MeV. All these were generated with a Gaussian fluctuation of the total energy with $\sigma = 80$ MeV, and with a Gaussian angular fluctuation with $\sigma = 170$ mrad around an offset of 100 mrad w.r.t. perpendicular incidence to the detector plane (the offset is to take into account the Earth's curvature). A sample of π^0's with the same characteristics was also produced.

The intensity of Cherenkov photons is proportional to $1/\lambda^2$, where λ is the photon wavelength. This spectrum is heavily distorted by the absorption properties of sea water, which is different from the absorption in sweetwater because of the salt content. The absorption length used in our simulations is the one measured by the ANTARES collaboration [19] and is shown in Fig. 11.

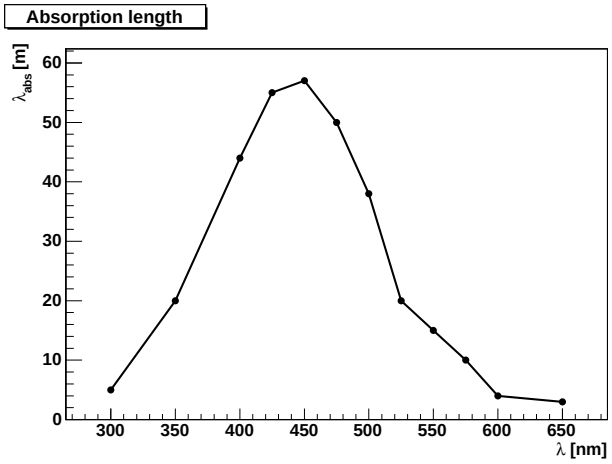

Figure 11: Light absorption length in sea water as a function of wavelength.

The spectral shape of Cherenkov photons will be different for different distances in sea water. Incidentally, for a typical distance of 20 m the resulting spectrum is well matched to the typical quantum efficiency of bialkali photocathodes [20], see Fig. 12.

For photon scattering, we adopted the procedures which are used by the ANTARES collaboration [19]. Each photon can undergo Mie scattering and Raleigh scattering, where Mie scattering occurs with a probability of 86%. The distribution of scattered photons is dominant in the forward direction for Mie scattering, but forward-backward symmetric for Raleigh scattering. The resulting overall distribution of scattering angles is shown in Fig. 13.

The last ingredient is the photon scattering length in sea water. Again following ANTARES, we adopted a linear parametrization of measurements at wavelengths $\lambda = 375$ and 475 nm:

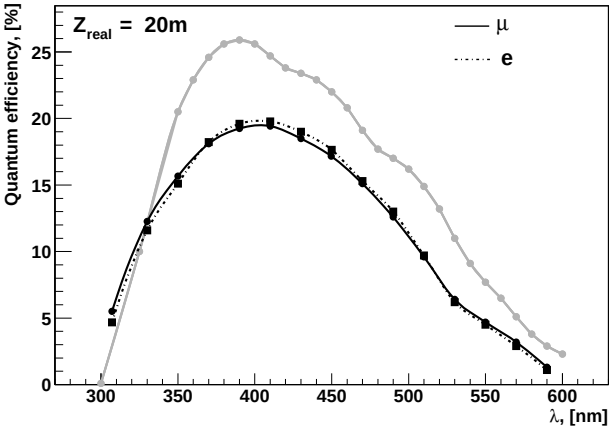

Figure 12: Light distribution as a function of wavelength, after absorption over more than 20 m of sea water; the typical quantum efficiency of a bialkali photocathode is superimposed.

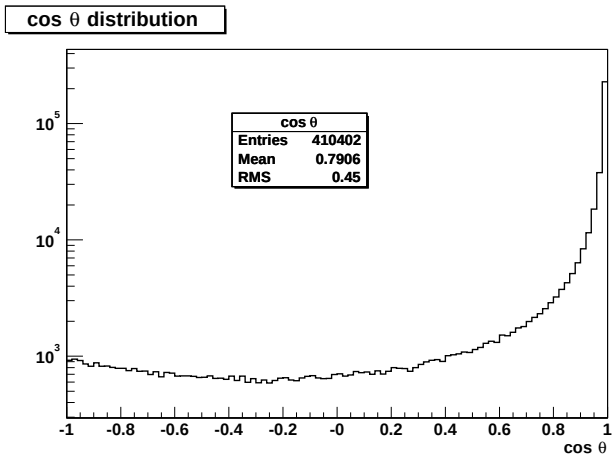

Figure 13: Cosine of photon scattering angle in sea water: superposition of forward-backward symmetric Raleigh scattering and forward Mie scattering.

$\lambda_{\rm scatt} = 53 + 0.265 \cdot (\lambda - 475)$. Thus, $\lambda_{\rm scatt}$ at $\lambda = 475$ nm is 53 m.

Table 2 gives the typical statistics of Cherenkov photons for 800 MeV electrons and muons: generated at the interaction vertex and after absorption and scattering for a distance of 20 m between vertex and detector plane. The number of photoelectrons when multiplied with the light collection efficiency of $\sim 8\%$ (see Section 5.1) and folded with the bialkali quantum efficiency (see Section 6) is also given.

Figure 14 shows the distribution of the distance of emission of Cherenkov photons from the vertex, for 800 MeV electrons and muons. While the distribution for electrons reflects the shape typical for an electromagnetic shower, the distribution for muons is flat and reflects the muon absorption length in water of ~ 3.5 m. Therefore, the detector plane will typically see Cherenkov rings with a width of ~ 3 m.

Table 2: Statistics of Cherenkov photons from 800 MeV electrons and muons

	electron	muon
generated	138000	104000
after absorption and scattering	37500	33300
photoelectrons	610	530

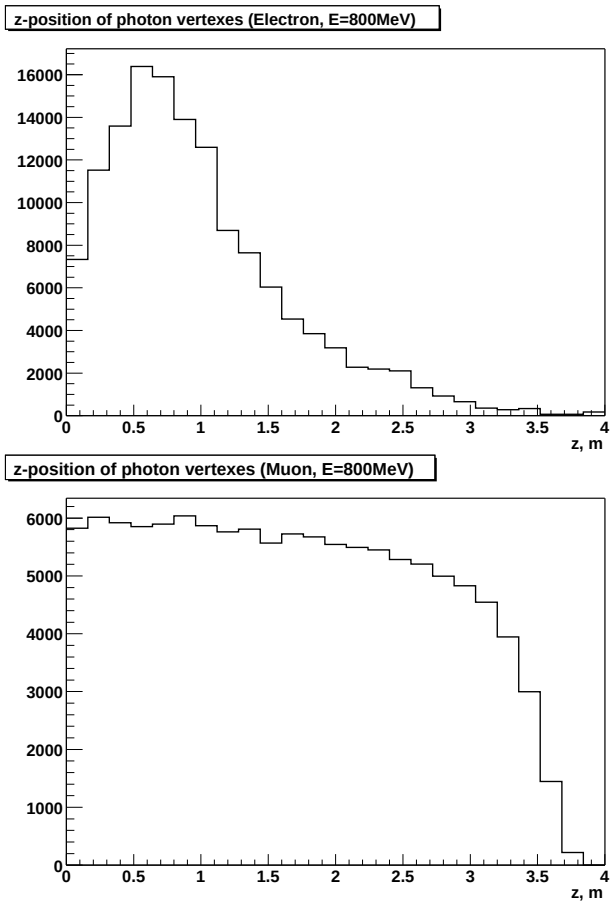

Figure 14: Distribution of the distance of emission of Cherenkov photons from the vertex, for 800 MeV electrons (top) and muons (bottom).

For the simulation of the measurement of the Cherenkov photons in the detector plane, the following key parameters were used:

- a basic grid of 3 m $\times$ 3 m was adopted: the amplitude created by the photons which fall, after due account of absorption and scattering, inside a circle of diameter 3 m was taken as spatial granularity (our simulation results suggest that a grid of 4 m $\times$ 4 m would not be appreciably worse); the requirement of falling inside the circle reduces the number of photons by a factor ~ 0.8 w.r.t. the grid's 3 m $\times$ 3 m area;
- this number of incoming photons was further reduced by a factor of 10 (this latter factor was originally motivated by the estimated light collection efficiency of a parabolic mirror),

and eventually folded with the quantum efficiency of a bialkali photocathode (Fig. 12); the angular response function was taken as flat, in quite some contrast to the actual angular response function of a mirror system, see Fig. 9; the resulting overall conversion factor of photons to photoelectrons is then $\sim 1.6\%$;

- to the resulting average number of photoelectrons an average background of 0.1 photoelectrons was added in each cell of the grid; the resulting sum served as mean value of a Poisson distribution of the observed number of photoelectrons.

Figure 15 shows the Cherenkov rings in terms of photoelectrons, of a typical electron (top) and muon (bottom) event with 800 MeV total energy, with the vertex located 20 m upstream of the detector plane. The geometrical 'fuzziness' of electron rings is evident in comparison with muon rings.

The time distribution of the arrival of photons is an important information as it reflects the spatial configuration of the event. Our simulation suggests that a timing resolution of ≤ 2 ns is adequate. Figure 16 shows the average time distribution of 10 electron and muon events each, from a vertex located 20 m upstream of the detector plane, where the arrival of the first photon is taken as time reference.

From the observed time distribution (with a 1 ns binning) and the knowledge of the photon velocity of 4.7 ns/m, it is possible to reconstruct the event vertex without prior knowledge of the event configuration, which is an important asset for event reconstruction. To illustrate this point, and to show the precision of vertex reconstruction in the most imprecise (longitudinal) coordinate, Fig. 17 shows the reconstructed longitudinal vertex coordinate for 800 MeV electrons and muons.

Knowing the vertex position, the total energy of the event can be reconstructed by correcting the energy observed in each cell by the attenuation due to the known path length of the light. Figure 18 shows the resulting difference between reconstructed and true energy. The achieved energy resolution of $\sim 7\%$ is very good, and supports *a posteriori* the choice of Cherenkov light in water as the detection technology.

A key requirement on the detector is its capability to separate electrons from muons, as this is centrally important for sensitivity to a small $\nu_\mu \rightarrow \nu_\mathrm{e}$ transition probability. In our simulation, we investigated two avenues:

- the 'amplitude' separation which depends on the distribution of amplitudes across cells with non-zero hits, and
- the 'fuzziness' separation which depends on the geometrical configuration of the cells with non-zero hits.

We note here the importance of being sensitive at the one photoelectron level (which was one motivation of our choice of the HPD as preferred photon detector over a traditional photomultiplier tube).

The amplitude separation rests on the observation that in a 'muon event' the energy is concentrated in less cells in comparison to 'electron events'. This is quantified in Fig. 19 which gives the average relative energy in the i.th non-zero cell when cells are ordered according to their energy content, for 800 MeV electrons and muons. The separation capability between electrons and muons resulting from the highest relative content in N cells is obvious. A closer inspection

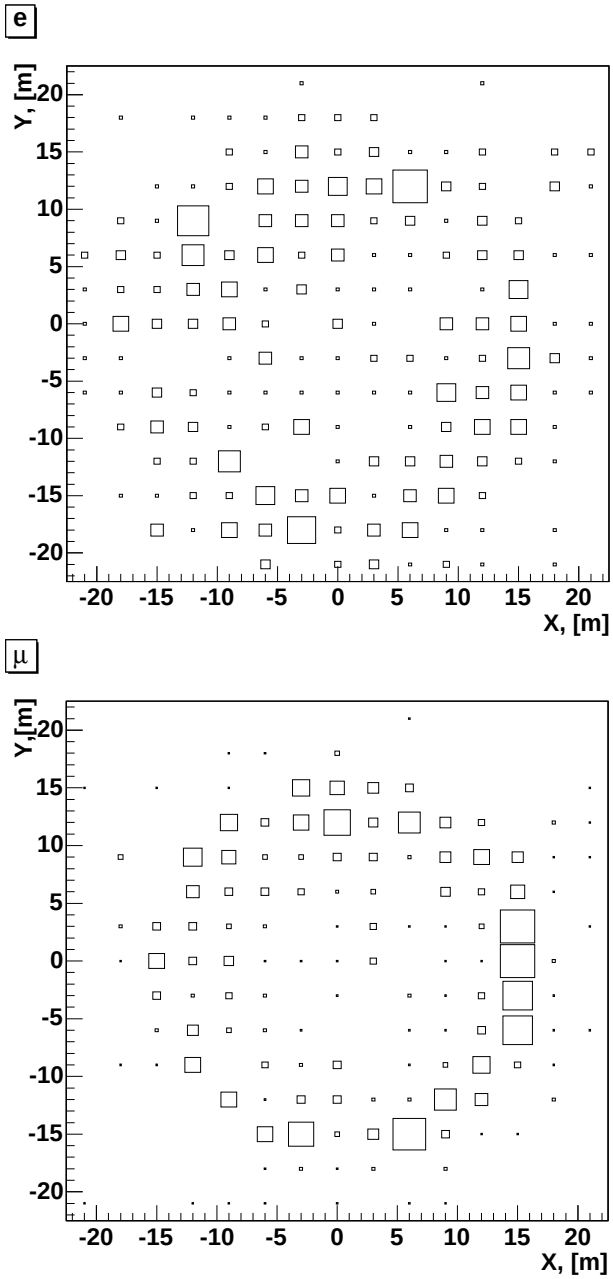

Figure 15: Cherenkov rings in terms of photoelectrons of a typical electron (top) and muon (bottom) event with 800 MeV total energy, with the vertex located 20 m upstream of the detector plane.

confirms what is expected: N will depend on the distance between vertex and detector plane (and may also depend on the level of background photoelectrons).

After optimizing N as a function of the distance between vertex and detector plane, the resulting separation between 800 MeV electrons and muons is shown in Fig. 20 as a function of the longitudinal vertex position (upper plot). The separation capability is satisfactory. Also shown in Fig. 20 is the purity of electrons as a function of their detection efficiency (lower plot): with

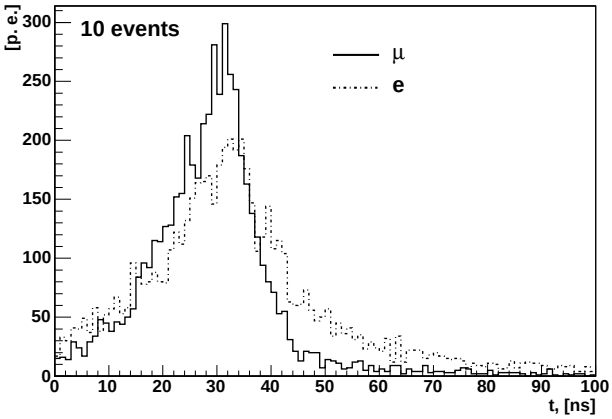

Figure 16: Time distribution of the arrival of photons from 800 MeV electrons and muons from a vertex located 20 m upstream of the detector plane.

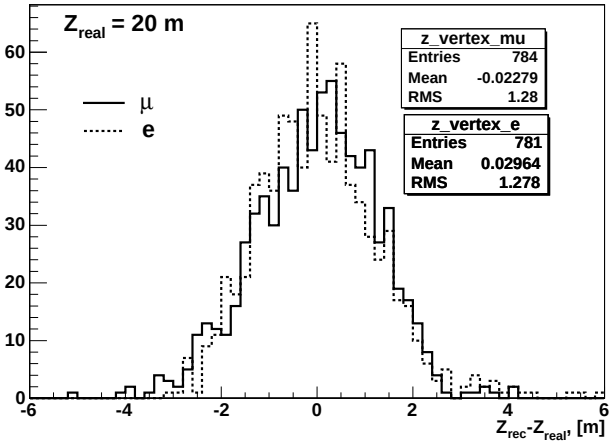

Figure 17: Reconstructed longitudinal vertex coordinate for 800 MeV electrons and muons.

a loss of 10% of the electrons, the probability of mis-identifying a muon as electron is 1×10^{-3}.

We note that up to this point the 'fuzziness' separation has not been employed. Since it is based on geometric information, its separation power is largely uncorrelated with the one from amplitude information. Thus it will aid the separation of electrons from muons, however our simulations indicate that its separation power is less powerful than the one from amplitude separation.

In our simulation, all neutrino-induced processes were generated with the program NEUGEN [15]. This program incorporates many details of low-energy neutrino interactions with nuclei (^{16}O in our case) such as nuclear form factors, Fermi motion, Pauli blocking, and re-interaction of secondary hadrons inside the nucleus. One consequence of this is that the quasi-elastic CC reaction with nucleons inside a nucleus is more complicated than the one with free nucleons: the angular distribution of the outgoing lepton broadens, and the energy distribution becomes asymmetric toward low energy. This is shown in Fig. 21, a scatter plot of the polar angle of muons from the

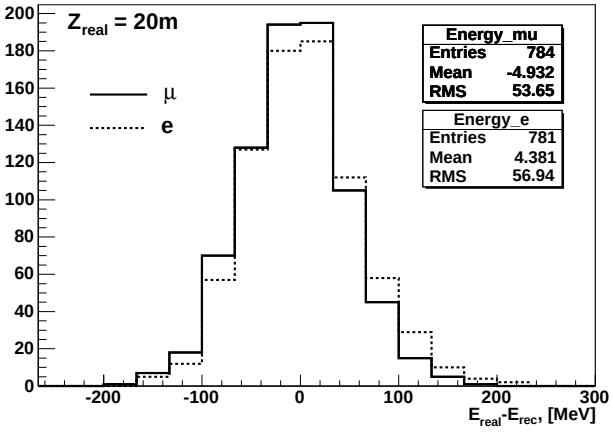

Figure 18: Energy resolution of 800 MeV electrons and muons.

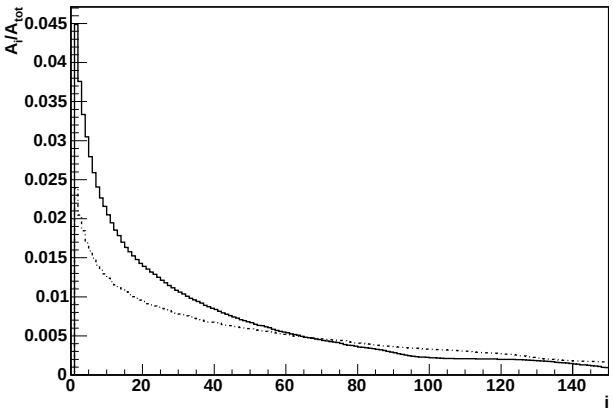

Figure 19: Average relative energy in the i.th non-zero cell when cells are ordered according to their energy content, for 800 MeV electrons (light) and muons (dark).

quasielastic reaction in the ^{16}O nucleus, versus muon momentum.

If all CC reactions (quasi-elastic, resonant π production and deep-inelastic scattering) are reconstructed with the kinematic model of quasi-elastic neutrino scattering off a free nucleon, Fig. 22 emerges. It shows the neutrino energy reconstructed from the energy and the polar angle of the final-state lepton. It appears that the quasi-elastic reaction can be well separated from background by selecting a lepton energy above $\sim$ 600 MeV.

After quasi-elastic CC ν_e scattering events are separated from background which involves final-state muons, the remaining challenge is the separation from NC-induced events. The most severe challenge is posed by π^0 production in NC interactions, where the π^0 decay into two photons is asymmetric and thus simulates a forward-going electron.

In NC reactions, π^0 can be produced resonantly off nucleons or coherently off the ^{16}O nucleus (for the cross-sections of these processes, see Fig. 6). For both processes, the scatter plots of the polar angle of the π^0 versus its momentum are shown in Fig. 23. The π^0 from coherent

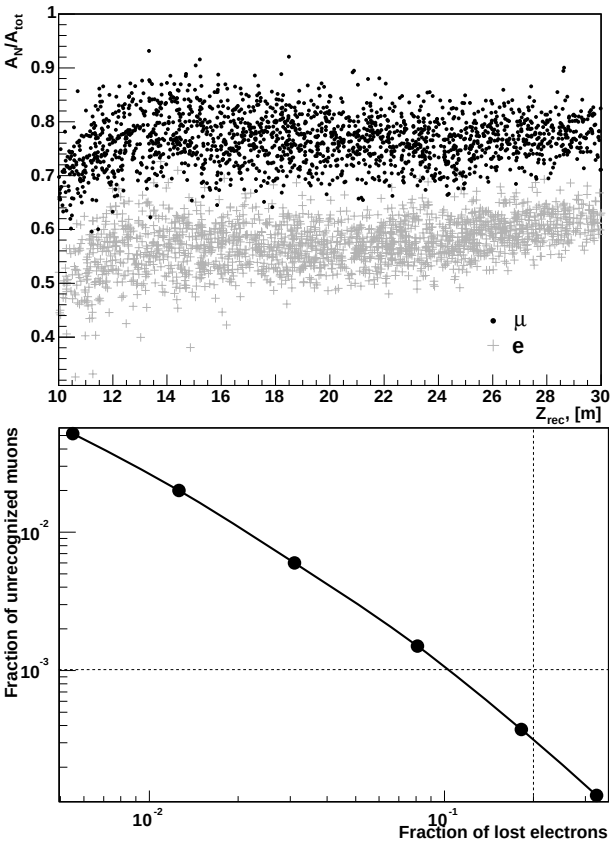

Figure 20: Separation of 800 MeV electrons and muons as a function of the reconstructed longitudinal vertex position (top); purity versus efficiency of the electrons with respect to muons (bottom); the separation is based on amplitude information only.

production are more dangerous, however the danger is mitigated by the low cross-section of this process. Altogether, the π^0 background with momentum greater than 600 MeV is 7×10^{-4} for resonant production, and 3×10^{-4} for coherent production, relative to the total CC cross-section per nucleon. These numbers do not include smearing effects due to energy resolution and hence will be worse in reality, yet do not pose a major problem.

Nevertheless, we studied the potential of separating the high-momentum tail of π^0's from 800 MeV electrons. The dangerous configuration is that one photon from π^0 decay goes forward and takes nearly all the energy so that the second photon escapes detection; on the other hand, the possibility of rejecting π^0 events exists when the geometrical configuration resembles a 2-ring rather than a 1-ring structure. On the basis of a combination of geometrical and amplitude information the separation between 800 MeV π^0 and electrons shown in Fig. 24 could be achieved. Losing $\sim 10\%$ of the electrons by a cut as shown in Fig. 24, would eliminate $\sim 70\%$ of the π^0's.

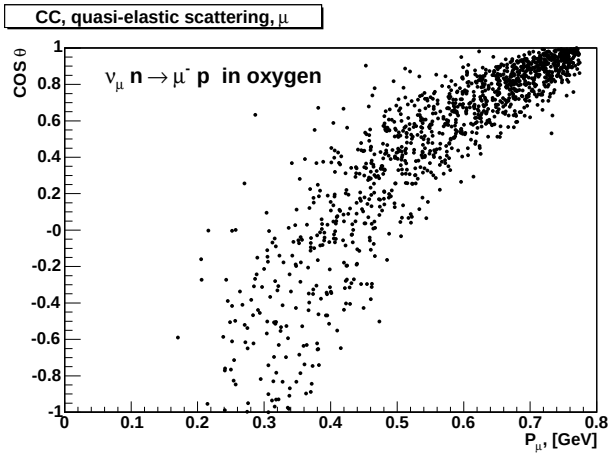

Figure 21: Cosine of the polar angle of muons from the quasielastic reaction in the ^{16}O nucleus, versus muon momentum.

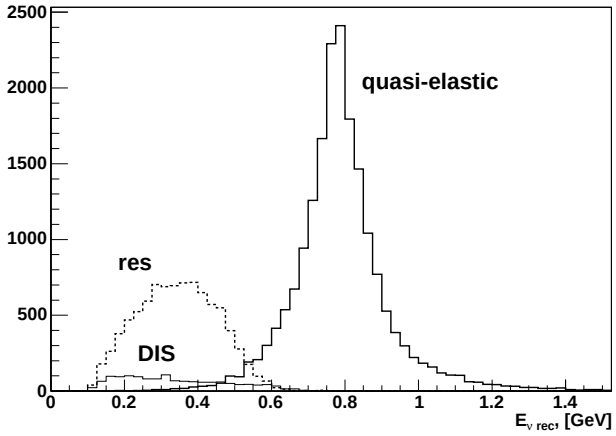

Figure 22: Neutrino energy reconstructed from events with a single muon under the hypothesis of quasieleastic neutrino-nucleon scattering.

7 Precision and sensitivity

7.1 Signal and background

The experiment makes use of two signals:

1. CC quasielastic $\nu_{\rm e}$ events with ~ 800 MeV visible energy;
2. CC quasielastic ν_μ events with ~ 800 MeV visible energy.

In the selection of both $\nu_{\rm e}$ and ν_μ signal events, the low-energy tail of the off-axis neutrino beam is removed by requiring $E_\nu^{\rm vis} > 600$ MeV. This cut eliminates at the same time quasielastic

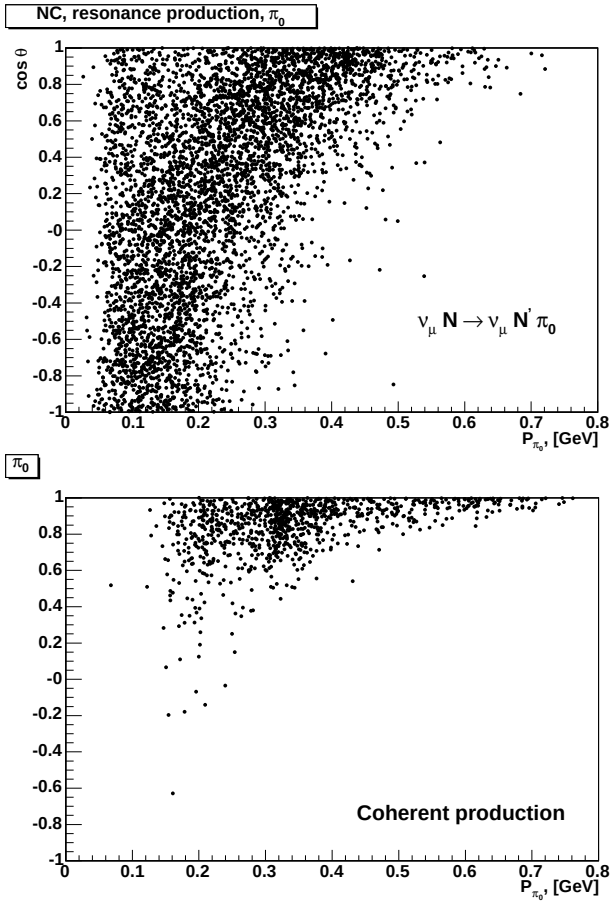

Figure 23: Cosine of the polar angle versus the π^0 momentum for π^0 production by neutral currents: resonant production (top) and coherent production on the ^{16}O nucleus (bottom).

events with large polar angles of the outgoing lepton.

The CC quasielastic ν_e sample is further reduced by cuts which suppress contamination by mis-identified CC quasielastic ν_μ events, and mis-identified NC events with a resonantly or coherently produced π^0.

Table 3 summarizes what our simulation studies suggest as reasonable signal efficiencies.

Table 3: Signal efficiencies after cuts

	CC quasielastic ν_e	CC quasielastic ν_μ
Removal of low-energy neutrinos	0.8	0.8
Removal of large-angle scattering	0.9	0.9
CC quasielastic ν_μ suppression	0.9	–
NC π^0 suppression	0.9	–
Overall	0.6	0.7

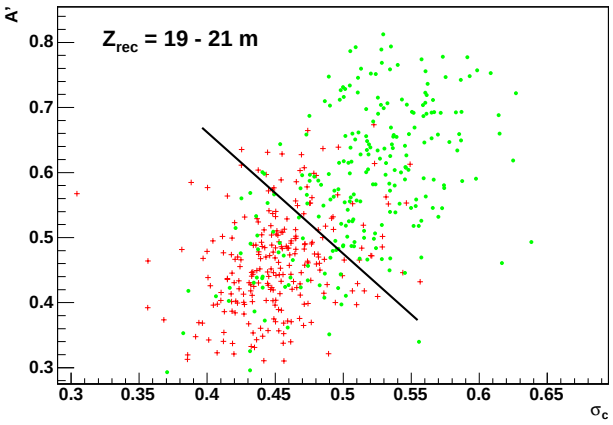

Figure 24: Separation between 800 MeV electrons (crosses/red) and π^0's (dots/green) by the amplitude and geometrical fluctuation criteria.

The signals will have backgrounds. In this context, it is important to note that the contamination of beam neutrinos from π decay by those from K decay matters only through its contribution to a flux of genuine ν_e events from K_{e3} decays.

Table 4 summarizes what our simulation studies suggest as reasonable estimates of the dominant backgrounds; they are given as percentage of the (unoscillated) CC quasielastic ν_μ signal events.

Table 4: Background percentages

	CC quasielastic ν_e	CC quasielastic ν_μ
ν_e from K_{e3} and μ decays	$(0.2 \pm 0.1)\%$	–
Misidentified CC quasielastic ν_μ events	$(0.1 \pm 0.05)\%$	–
π^0 from NC production	$(0.1 \pm 0.05)\%$	–
$\pi^\pm$ from resonant NC production	–	0.1%
Sum of backgrounds	$(0.4 \pm 0.1)\%$	0.1%

There will be a continuous background from ^{40}K decays, and intermittent light from biological activity (bio-luminescence). The ^{40}K background which is of order 50 kHz per cell, translates into 0.005 per 100 ns and hence poses no problem. Spells of bioluminescence may enforce temporary suspension of data taking.

No problems arise from cosmic-ray background since the readout is limited to the accelerator spill which gives a reduction by a factor of $\sim 10^5$ with respect to continuous sensitivity.

7.2 Δm^2_{23} and θ_{23}

In the absence of precise knowledge of Δm^2_{23}, but guided by all experimental input available then, the experiment will be located at three different positions along the beam, optimally spaced for achieving the best precision on Δm^2_{23} and θ_{23}.

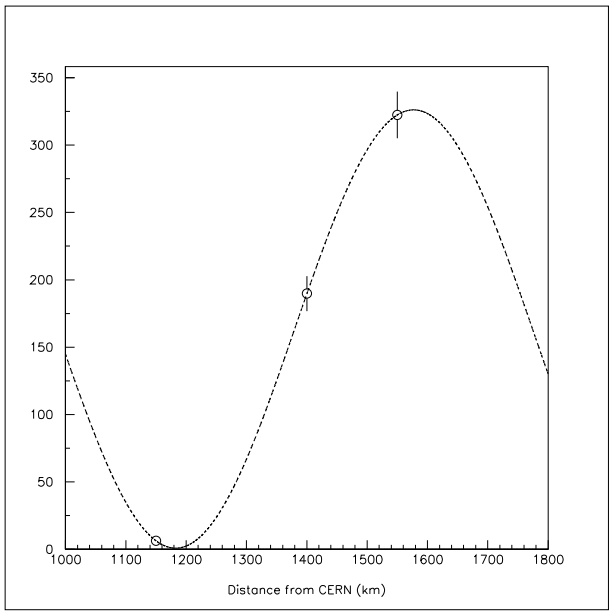

Figure 25: Fit of the CC quasielastic ν_μ rates at three different baselines in terms of $\sin^2\theta_{23}$ and Δm^2_{23}; two points correspond to one year of data taking each, the point near the minimum uses the full statistics from five years of data taking.

Fig. 25 shows the CC quasielastic ν_μ rates at three different baselines fitted in terms of $\sin^2\theta_{23}$ and Δm^2_{23}. For this plot, it was assumed that one year of data taking would be spent at two of the three locations, and five years at the 2nd oscillation maximum (where the ν_μ rate is at its minimum). The relative normalization between the event numbers at the three locations is achieved from the muon flux in the shield after the decay tunnel at CERN, the statistical error of which is negligible compared to the event statistics.

Table 5 gives the numerical results for the errors of the fit parameters. While the precision on $\sin^2\theta_{23}$ is modest, Δm^2_{23} is measured with excellent precision.

Table 5: Precision of $\sin 2\theta_{23}$ and Δm^2_{23}.

error on $\sin^2\theta_{23}$	$\sim 8\%$
error on Δm^2_{23}	$\sim 1\%$

Early information from the three positions will define the exact position for five years of data-taking at the position with maximum sensitivity on the transition $\nu_\mu \rightarrow \nu_e$, and hence on the currently most important oscillation parameter $\sin^2\theta_{13}$.

7.3 θ_{13}

Table 6 gives a summary of the relevant parameters and expected results from the five-year data taking at the 2nd ν_μ oscillation maximum. The limits given include our estimate of the

systematic experimental error.

Table 6: Summary of C2GT parameters and expected results from five years of running at the 2nd ν_μ oscillation maximum in search of $\nu_\mu \rightarrow \nu_e$ transitions.

Radius of instrumented detector disc [m]	150
Height of cone of fiducial volume [m]	30
Fiducial mass [Mt]	1.5
No. of 400 GeV/c protons per year on target	5×10^{19}
No. of useful π^+ decays per proton on target	0.5
Years of running at oscillation maximum	5
No. of ν_μ CC interactions (unoscillated)	3388
No. of ν_μ CC quasielastic interactions (unoscillated)	2181
CC quasielastic ν_μ selection efficiency	0.7
No. of CC quasieleastic ν_μ events after cuts (unoscillated)	1527
No. of background events for the ν_e signal	8.7
Systematic error on background events	30%
CC quasielastic ν_e selection efficiency	0.6
Discovery potential (3σ) on $\nu_\mu \rightarrow \nu_e$ probability	0.0077
Discovery potential (3σ) on $\sin^2\theta_{13}$	0.0039
Discovery potential (3σ) on $\sin^2 2\theta_{13}$	0.0154
Upper limit (90% CL) on $\nu_\mu \rightarrow \nu_e$ probability	**0.0033**
Upper limit (90% CL) on $\sin^2\theta_{13}$	0.0016
Upper limit (90% CL) on $\sin^2 2\theta_{13}$	0.0066
No. of ν_e observed signal events for $\sin^2\theta_{13} = 0.05$	131

We wish to point out that the direct experimental result is the $\nu_\mu \rightarrow \nu_e$ transition probability at the 2nd $\nu_\mu$oscillation maximum. While the number of ν_e signal events is measured in the long-time exposure, the (unoscillated) number of ν_μ events must be inferred from the measurements at all three locations.

In Table 6, this transition probability has been converted into $\sin^2\theta_{13}$ and $\sin^2 2\theta_{13}$, respectively, using Eq. 3. It is understood that this approach is too simplistic since it does not take proper account of theoretical uncertainties and ambiguities arising from the unknown mass hierarchy of neutrino mass eigenstates (hierarchical or inverted), and of possible CP violation effects.

We also emphasize that the final sensitivity of the experiment must be re-assessed after completion of the following studies:

- a realistic beam energy spectrum obtained after the engineering design of the target and the subsequent focussing devices;
- a realistic photon detection system;
- a detailed simulation of all kinds of resolution effects and backgrounds;
- inclusion of theoretical ambiguities mentioned above, and correlations with uncertainties of Δm^2_{23} and θ_{23};
- optimization of the data collection strategy with a view to reducing the above ambiguities;

this will involve a study of the time to be spent at each detector location and a possible split between neutrino and antineutrino running.

7.4 Comparison with competing projects

The most advanced competing project is T2K [21] in Japan which will send a neutrino beam from the new 50 GeV synchrotron at JPARC, under construction, to SuperKamiokande. It will use the off-axis technique to select the right momentum band to be at oscillation maximum. Present planning makes it ready in 2009. Its base line of 295 km makes it unsuitable to address the mass hierarchy through matter effects. Based on a 5 year run they estimate a 3σ discovery potential of ~ 0.006 on the $\nu_\mu \to \nu_\mathrm{e}$ oscillation probability which, given the ambiguities introduced by the mass hierarchy and the CP-violating phase δ, they translate to an upper limit of 0.0015 at 90% CL on $\sin^2\theta_{13}$.

The NOνA project [22] at Fermilab also uses the off-axis technique. It plans to use the NuMI beam that will be operational at the end of 2004 and proposes to build a new detector of about 50 kt at about 800 km from Fermilab in Minnesota in the direction of the Soudan mine used by MINOS. A longer baseline and a higher energy accelerator makes it more suitable than the JPARC project to study the mass hierarchy and to use antineutrinos as well as neutrinos. The Fermilab Program Advisory Committee has given the NOνA project a strong endorsement and R&D funds but no final approval yet. Taking into account the ambiguities introduced by the mass hierarchy and the CP-violating phase δ, NOνA claims for 'Phase 1' an upper limit in the range 0.0011 – 0.0021 at 90% CL on $\sin^2\theta_{13}$.

Reactor experiments can also, as did CHOOZ, attempt to measure θ_{13}. Several projects are being discussed, the most advanced one being Double-CHOOZ [23] using two detectors, a far detector in the old CHOOZ cavern and a near one used to reduce systematic uncertainties, arising from the flux. Reactor projects, while measuring θ_{13} with no ambiguities, are limited by systematics and cannot address the mass hierarchy or CP violation. The Double-CHOOZ upper limit is 0.0125 at 90% CL on $\sin^2\theta_{13}$, for a three-year run.

8 R&D programme, on-site studies

There are two outstanding issues which need a vigorous R&D programme:

- construction and testing of an HPD; this programme has been started already with the design and fabrication, at CERN, of prototypes with a smaller diameter; the smaller than final diameter (210 mm rather than the envisaged 380 mm) is imposed by the use of existing equipment;
- on-site measurements of sea water properties in 1000 m depth: velocity of water currents, light absorption and scattering, sedimentation, residual background from daylight, bioluminescence, ^{40}K background.

9 Summary

An experiment in the Gulf of Taranto is proposed which exploits the coincidence between a suitably located deep-water trench aligned with the CNGS beam, a strong sensitivity to oscillation parameters when exploiting three locations of order 100 km apart along the beam line, and a monochromatic 800 MeV neutrino beam in the natural off-axis configuration of the CNGS beam, whose energy is below the tau-production threshold and thus reduces background.

The envisaged detector is a water Cherenkov detector at a depth of 1000 m. It has a fiducial mass of 1.5 Mt. The light-detecting elements are located on a disc with radius 150 m, oriented perpendicularly to the neutrino beam. The detector is moveable and is anchored at three different distances from CERN.

The experiment confirms unambiguously the oscillatory pattern, neutrino flavour transitions, measures the atmospheric oscillation parameters θ_{23} with modest and Δm^2_{23} with excellent precision, and is sensitive to a value of θ_{13} much smaller than the current upper limit.

The experiment uses instrumentation which is largely understood, thanks to the pioneering R & D work first of DUMAND, then of LAKE BAIKAL, and then of ANTARES, NEMO and NESTOR.

Overall, the experiment appears both worthwhile and feasible. Important challenges are (i) the highest possible neutrino flux, (ii) maximal efficiency of collecting Cherenkov light in water, and (iii) maximal reduction of background events which fake CC quasielastic ν_e events with 800 MeV energy.

Acknowledgements:
This work has been helped a lot by friendly expert advice from members of the NEMO and NESTOR Collaborations, and especially of the ANTARES Collaboration. We are greatly indebted to A. Broncano and O. Mena who contributed a great deal to early conceptual studies.

References

[1] Z. Maki, M. Nakagawa and S. Sakata, Prog. Theor. Phys. **28** (1962) 970;
Particle Data Group, Review of Particle Physics, Eur. Phys. J. **C3** (1998) 1 (The convention for the sign of δ used in the text is opposite to the one used in this reference).

[2] Y. Fukuda *et al.*, Phys. Rev Lett. **81** (1998) 1562; Phys. Lett. **B433** (1998) 9; *ibid.* **B436** (1998) 25; E. Kearns, Atmospheric Neutrino Results from Super-K, talk presented at the Neutrino 2004 Conference, June 2004, Paris (France) (*http://neutrino2004.in2p3.fr*).

[3] S. Goswami, Global Analysis of Neutrino Oscillation, talk presented at the Neutrino 2004 Conference, June 2004, Paris (France) (*http://neutrino2004.in2p3.fr*).

[4] J.F. Wilkerson, The Sudbury Neutrino Observatory, talk presented at the Neutrino 2004 Conference, June 2004, Paris (France) (*http://neutrino2004.in2p3.fr*).

[5] G. Gratta, New Results from KamLAND, talk presented at the Neutrino 2004 Conference, June 2004, Paris (France) (*http://neutrino2004.in2p3.fr*).

[6] M. Apollonio *et al.*, Phys. Lett. **B466** (1999) 415.

[7] M. Thomson, Status of NuMI/MINOS, talk presented at the Neutrino 2004 Conference, June 2004, Paris (France) (*http://neutrino2004.in2p3.fr*).

[8] A. Aguilar *et al.*, Phys. Rev. **D64** (2001) 112007.

[9] A.K. Mann, Proc. 3rd NESTOR International Workshop, Pylos, Greece, 1993 (ed. L.K. Resvanis), p. 385.

[10] R.L. Helmer, Proc. 9th Lake Louise Winter Institute, Lake Louise, Canada, 1994 (World Scientific, 1995; eds. A. Astbury *et al.*), p. 291.

[11] D. Beavis *et al.*, Long Baseline Neutrino Oscillation Experiment at the AGS (Proposal E889), Physics Design Report BNL 52459 (1995).

[12] L.K. Resvanis (NESTOR Collaboration), private communication.

[13] G. Acquistapace et al., The CERN neutrino beam to Gran Sasso (NGS), Report CERN 98–02 and INFN/AE-98/05; Addendum CERN SL-99-034 DI and INFN/AE-99/05.

[14] We thank F. Pietropaolo for making his neutrino beam codes available for our studies.

[15] The program NEUGEN was developed and used in the Soudan-2 and MINOS collaborations (*http://minos.phy.tufts.edu/gallag/neugen*).

[16] B. Massey, Mechanics of Fluids, 7th ed., Stanley Thornes Publishing Co., Cheltenham, UK.

[17] C. Joram, Hybrid Photodiodes, Nucl. Phys. (Proc. Suppl.) **B78** (1999) 407.

[18] A.Braem *et al.*, Technology of photocathode production, NIM **A502** (2003) 205.

[19] J.A. Aguilar *et al.*, Transmission of light in deep sea water at the site of the ANTARES neutrino telescope, preprint subm. to Astrop. Phys.; see also the Proc. of the VLVνT Workshop held at NIKHEF, Amsterdam, October 2003 (*http://www.vlvnt.nl*).

[20] We adopted the typical spectral response of the photomultiplier tube R1828-01 from HAMAMATSU.

[21] Y. Hayato, T2K: long baseline neutrino experiment at J-PARC, talk presented at the Neutrino 2004 Conference, June 2004, Paris (France) (*http://neutrino2004.in2p3.fr*)

[22] M. Messier, The NOνA Experiment, talk presented at the Neutrino 2004 Conference, June 2004, Paris (France) (*http://neutrino2004.in2p3.fr*)

[23] L. Oberauer, θ_{13} Measurements at Reactors, talk presented at the Neutrino 2004 Conference, June 2004, Paris (France) (*http://neutrino2004.in2p3.fr*)